Journal of Biomedical Optics

BiomedicalOptics.SPIEDigitalLibrary.org

Mapping absolute tissue endogenous fluorophore concentrations with chemometric wide-field fluorescence microscopy

Zhang Xu
Michael Reilley
Run Li
Min Xu

SPIE.

Zhang Xu, Michael Reilley, Run Li, Min Xu, "Mapping absolute tissue endogenous fluorophore concentrations with chemometric wide-field fluorescence microscopy," *J. Biomed. Opt.* **22**(6), 066009 (2017), doi: 10.1117/1.JBO.22.6.066009.

Mapping absolute tissue endogenous fluorophore concentrations with chemometric wide-field fluorescence microscopy

Zhang Xu,[a] Michael Reilley,[b] Run Li,[c] and Min Xu[b,*]
[a]Wenzhou Medical University, The Second Affiliated Hospital and Yuying Children's Hospital, Department of Pediatrics, Wenzhou, China
[b]Fairfield University, Department of Physics, Fairfield, Connecticut, United States
[c]Fairfield University, Department of Mechanical Engineering, Fairfield, Connecticut, United States

Abstract. We report chemometric wide-field fluorescence microscopy for imaging the spatial distribution and concentration of endogenous fluorophores in thin tissue sections. Nonnegative factorization aided by spatial diversity is used to learn both the spectral signature and the spatial distribution of endogenous fluorophores from microscopic fluorescence color images obtained under broadband excitation and detection. The absolute concentration map of individual fluorophores is derived by comparing the fluorescence from "pure" fluorophores under the identical imaging condition following the identification of the fluorescence species by its spectral signature. This method is then demonstrated by characterizing the concentration map of endogenous fluorophores (including tryptophan, elastin, nicotinamide adenine dinucleotide, and flavin adenine dinucleotide) for lung tissue specimens. The absolute concentrations of these fluorophores are all found to decrease significantly from normal, perilesional, to cancerous (squamous cell carcinoma) tissue. Discriminating tissue types using the absolute fluorophore concentration is found to be significantly more accurate than that achievable with the relative fluorescence strength. Quantification of fluorophores in terms of the absolute concentration map is also advantageous in eliminating the uncertainties due to system responses or measurement details, yielding more biologically relevant data, and simplifying the assessment of competing imaging approaches. [DOI: 10.1117/1.JBO.22.6.066009]

Keywords: endogenous fluorescence; chemometric microscopy; spatial distribution; fluorophore concentration; nonnegative factorization; spatial diversity.

Paper 160765RR received Nov. 7, 2016; accepted for publication May 30, 2017; published online Jun. 15, 2017.

Light interaction with tissue and cells can be used to quantify their biochemical, functional, and morphologic properties noninvasively and has permeated biology and medicine.[1,2] Among different optical methods, fluorescence, in particular, reveals the biochemical and molecular environments. For example, autofluorescence from intrinsic molecules has been demonstrated to be an effective probe for tissue physiological state[3–12] and used to monitor cellular metabolism to differentiate normal, dysplasia, and cancer *ex vivo* and *in vivo*.[13–20] Imaging endogenous fluorescence typically requires a confocal microscope with laser excitation owing to its weak strength, which hinders its wider applications. In this paper, we present a chemometric fluorescence microscopy that uses broadband excitation and detection to dramatically increase the signal-to-noise ratio (SNR) in wide-field fluorescence imaging and further resolves and maps the absolute concentration of individual fluorescent intrinsic molecules by computational synthesis.

Consider a specimen of thickness L (such as a pathology slide whose $L \sim 4$ μm) with endogenous fluorophore concentrations of $c_j(x,y)$ with $1 \le j \le n$ denoting the j'th species and x, y being the lateral coordinates. Under broadband excitation and detection, the fluorescence intensity under one specific i'th combination of the excitation and detection bands can be written as $I_i = \sum_j w_{ij} c_j(x,y)$ with

$$w_{ij} = \int E_i(\lambda_e) X_i(\lambda_x) S(\lambda_e, \lambda_x) f_j(\lambda_e, \lambda_x) L \mathrm{d}\lambda_e \mathrm{d}\lambda_x, \tag{1}$$

where $\lambda_{e,x}$ are the emission and excitation wavelengths, respectively, E_i and X_i are the emission and excitation bands for the i'th configuration (channel) with $1 \le i \le m$ and m being the total number of channels, S is the system response function, and f_j is the excitation–emission spectrum for the j'th species. The total fluorescence signal from the j'th species across all channels is given by

$$C_j = \sum_i w_{ij} c_j(x,y) = K_j c_j(x,y), \tag{2}$$

where $K_j \equiv \sum_i w_{ij}$ represents the total fluorescence intensity across all channels produced by one unit of the j'th species of fluorophore. The fluorescence signal can then be written as

$$\begin{pmatrix} I_1 \\ I_2 \\ \\ I_m \end{pmatrix} = \begin{pmatrix} w_{11} & w_{12} & w_{1n} \\ w_{21} & w_{22} & w_{2n} \\ & & \\ w_{m1} & w_{m2} & w_{mn} \end{pmatrix} \begin{pmatrix} c_1 \\ c_2 \\ \\ c_n \end{pmatrix} = \begin{pmatrix} \bar{w}_{11} & \bar{w}_{12} & \bar{w}_{1n} \\ \bar{w}_{21} & \bar{w}_{22} & \bar{w}_{2n} \\ & & \\ \bar{w}_{m1} & \bar{w}_{m2} & \bar{w}_{mn} \end{pmatrix} \begin{pmatrix} C_1 \\ C_2 \\ \\ C_n \end{pmatrix}, \tag{3}$$

*Address all correspondence to: Min Xu, E-mail: mxu@mail.fairfield.edu

1083-3668/2017/$25.00

or, in short, $\mathbf{I} = W\mathbf{c} = \bar{W}\mathbf{C}$, where the normalized weights $\bar{w}_{ij} \equiv w_{ij}/K_j \geq 0$ and $\sum_i \bar{w}_{ij} = 1$. The weights $\bar{w}_{ij}$ $(i = 1,2,\ldots,m)$ can be regarded as the spectral signature (feature) of the j'th component. The weights $\bar{w}_{ij}$ and the strength K_j are completely determined by the fluorophore species and the imaging system configuration alone.

When the species of the fluorophore are known *a priori*, the weighting matrix w_{ij} can be directly measured under the identical experimental condition. A pixel-by-pixel regularized inversion[21] can then be used to infer $\mathbf{C}$ from $\mathbf{I}$ in either over-determined $(m \geq n)$ or under-determined $(m < n)$ cases. There are, however, a few drawbacks for such approaches, including the need for the exact knowledge of number and types of fluorescent species and their signatures in the medium and the possibility of generating unphysical negative values for the concentration. The issue is further compounded by spectral shifts and signature variations between pure fluorophores and fluorophores in the specimen owing to their different biochemical environments.

The spatial diversity of the wide-field fluorescence image allows a second more attractive approach by learning the parts (fluorophores) directly from the data through nonnegative matrix factorization (NMF).[22] Denoting the total number of pixels in the microscopic image as $N = N_x N_y$ with $N_{x,y}$ being the x, y dimension of the image, respectively, the measured fluorescence intensity vector $\mathbf{I}^{(k)}$ on the k'th pixel (x_k, y_k) satisfies Eq. (3), and stacking these $\mathbf{I}^{(k)}$'s $(1 \leq k \leq N)$ yields

$$V = \bar{W}H + \varepsilon, \tag{4}$$

where $V = [\mathbf{I}^{(1)}, \mathbf{I}^{(2)}, \ldots, \mathbf{I}^{(N)}]$, $H = [\mathbf{C}^{(1)}, \mathbf{C}^{(2)}, \ldots, \mathbf{C}^{(N)}]$, and ε is an $m \times N$ matrix representing measurement noise. Noting that $N \gg m, n$, NMF provides an efficient method factorizing the data cube V of dimension $m \times N$ into a feature matrix $\bar{W}$ of dimension $m \times n$ and a coefficient matrix H of dimension $n \times N$, where V, $\bar{W}$, and H are all nonnegative matrices. The basic principle of NMF is to iteratively seek nonnegative matrices $\bar{W}$ and H to minimize a functional such as the squared error $\|V - \bar{W}H\|_F^2$.[22,23] After NMF of V, the normalization condition for the feature matrix $\bar{W}$ is enforced by dividing the j'th column of $\bar{W}$ by $\sum_i \bar{w}_{ij}$ and multiplying the corresponding j'th row of H by the same factor. The j'th row of the final coefficient matrix H then represents the two-dimensional (2-D) concentration map $C_j(x, y)$ of a fluorescent species with the corresponding j'th column in $\bar{W}$ being its spectral signature. If a bank of "pure" fluorophore candidates is available, their spectral signatures and strengths can be measured under the identical experimental condition. By matching (which needs not be identical) the spectral signature $\bar{w}_{ij}$ $(1 \leq i \leq m)$ to those from the bank (and further constrained by *a priori* information on their spatial distribution characteristics, if present), one can identify the fluorescent species for the j'th component and determine the fluorophore strength K_j. The absolute concentration map for the j'th species is then given by $c_j(x, y) = C_j(x, y)/K_j$. This NMF-based method is robust with respect to fluorescence spectral broadening or shifts. The spectral signatures of the fluorophores inside the biological tissue need not to be known exactly *a priori* and are retrieved together with the concentration maps simultaneously through NMF.

We will now present chemometric autofluorescence imaging of thin tissue sections as one example. Specific contributing fluorophores for tissue endogenous fluorescence include aromatic amino acid residues such as tryptophan found in most proteins ($\lambda_{ex} = 200$ to 340 nm, $\lambda_{em} = 360$ to 370, 455 nm); reduced pyridine nucleotides [NAD(P)H], which are cofactors in cellular metabolism and are found mainly in mitochondria but are also present in the cytoplasm ($\lambda_{ex} = 360$ nm, $\lambda_{em} = 460$ nm);[24] and flavins and flavin nucleotides (riboflavin, flavin mononucleotide, and dinucleotide), which are mostly bound to enzymes as coenzymes of flavoproteins and concentrated in the mitochondria ($\lambda_{ex} = 360$, 445 to 470 nm, $\lambda_{em} = 440$, 520 nm).[25] Extracellular matrix components collagen and elastin also contribute strongly to tissue native fluorescence.

An epi-fluorescence microscope (Axio 40cfl, Zeiss) was used to image an unstained paraffin embedded lung cancer tissue matrix array (TMA) (BioMax). Fresh surgically removed samples, within 15 to 30 min after surgical resection, were preserved in neutral phosphate buffered formalin (NBF) for 24 h before they were processed in a tissue processor (Leica) and embedded in paraffin. The light source was a 50-W mercury arc lamp. Tissue fluorescence images under UV excitation (using a UV fluorescence filter set with the excitation wavelength centered at 365 nm with a bandwidth of 12 nm) and blue illumination (using a filter set with the excitation wavelength centered at 480 nm with a bandwidth of 40 nm) were recorded by a digital camera (Canon 5D Mark II). Such broadband excitation and emission spectral imaging achieves sufficient SNR for the weak fluorescence signal. The channels in this setup are UV-R, UV-G, UV-B (under UV excitation), and B-R, B-G (under blue excitation) with $m = 5$. The exposure time was set at 1.5 s for both excitations. A bank of slides containing a thin uniform layer (~4-μm thick) of pure fluorophores (including tryptophan, collagen, elastin, nicotinamide adenine dinucleotide (NADH), flavin adenine dinucleotide (FAD), and porphyrin) water solution or suspensions was prepared separately and measured under the identical experimental condition. The B-R and B-G channels were multiplied by four for both specimens and the fluorophore bank to avoid the dominance of UV channels. Note that strong tryptophan fluorescence was excited in both the pure tryptophan sample and the tissue specimens under UV excitation although the illumination light is off its excitation peak (280 nm). Fixation causes cross linking in proteins; therefore, fixed tissue can be preserved for a relatively long time without incurring significant changes in the microenvironments. Fixation with NBF has been shown not to cause significant fixative-induced fluorescence.[26] The presence of fixative-induced fluorescence, if any, is accounted for as part of the noise ε in the fluorescence measurement [see Eq. (4)]. The fluorescence spectra of NADH and FAD seem to be unaffected by fixation with formalin,[27] and useful NADH and FAD measurements can be obtained from fixed tissue.[28,29] We have also observed the excitation and emission matrix measured for native fluorophores in fixed tissue to be similar to the ones being reported for fresh tissues.[8,12,17] No fluorescence from paraffin was observed. The selection of the UV band also preferably excites elastin rather than collagen. We note that, although the endogenous fluorescence spectra in appropriately fixed tissue are similar to those of intact tissue, fixed tissue may show stronger autofluorescence intensity than intact tissue owing to factors such as volume shrinkage. The study of autofluorescence from fixed tissue, however, suits the purpose of validation here and is itself of great interest. Histopathologic evaluations of fixed tissue are currently the gold standard for diagnosis, and the autofluorescence from fixed tissue promises great diagnosis potential.[29]

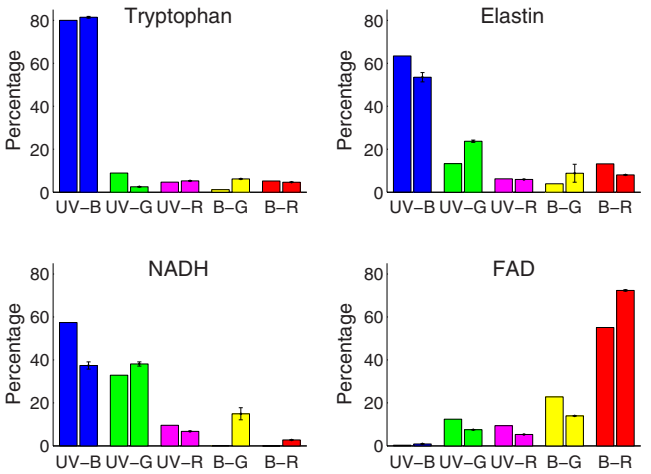

Fig. 1 The spectral signature of the extracted fluorescence components agree well with those measured for the "pure" fluorophore bank. "UV-B," "UV-G," and "UV-R" are the blue, green, and red channels, respectively, under the UV excitation. "B-G" and "B-R" are the green and red channels, respectively, under the blue excitation. The spectrum is normalized to one. The spectrum of the extracted fluorescence components is displayed to the right of that of the "pure" fluorophore bank. The error bars show the standard deviation for the spectral signature of the extracted fluorescence components across all specimens.

For each specimen, the block principal pivoting NMF algorithm[30] aided by spatial diversity decomposed the set of measured fluorescence images after background removal into a product of $\bar{W}$ and H. The distribution of individual fluorescence component is contained in one row of H and the fluorescence species is identified using the feature matrix $\bar{W}$. Figure 1 shows the spectrum of the extracted fluorescence components to the right of those measured for the "pure" fluorophore bank. The error bars show the standard deviation for the spectral signature of the extracted fluorescence components across all specimens. The red channel of the digital camera is also sensitive to green light, giving rise to an enhancement in the red channels,[31] most evident in the strong B-R channel for FAD. The spectral signature of the extracted fluorescence components overall agrees well with those from the "pure" fluorophore bank. The difference in the extracted and "pure" fluorescence spectra can be attributed to their different chemical environments. Note that the spectral signature of collagen (data not shown) is similar to that of elastin. The content of collagen and elastin in human lungs is also similar.[32] Although both collagen and elastin are present in the lung tissue specimen, the detected fluorescence is primarily from elastin with the current system as elastin is preferably excited under the chosen UV band with a ratio of 64:1 for the fluorescence intensity per unit mass between elastin and collagen.

The major fluorescence species are then identified to be Trp (tryptophan), elastin, NADH, and FAD. The fluorescence intensities of these four major components are significantly different between normal ($n = 36$), perilesional ($n = 30$), and cancerous ($n = 52$) lung tissue (see Fig. 2). The concentrations (mM) of Trp, elastin, NADH, and FAD and the redox ratios (concentration ratios) FAD/Trp and FAD/NADH measured for normal, perilesional, and cancerous lung tissue are summarized in Table 1. Note that the concentrations are for fixed lung tissue (TMA) and may overestimate those of fresh lung tissue. Tryptophan, elastin, NADH, and FAD are all observed to decrease significantly

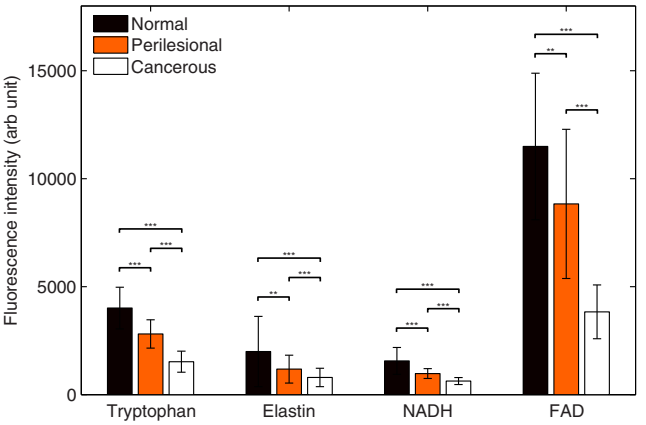

Fig. 2 The absolute fluorescence intensities differ significantly between normal ($n = 36$), perilesional ($n = 30$), and cancerous ($n = 52$) lung tissue. The significance is presented by "*" ($p < 0.05$), "**" ($p < 0.01$), and "***" ($p < 0.001$).

in their concentration from normal, perilesional, to cancerous lung tissue. The redox ratios (FAD/Trp and FAD/NADH) are observed to follow a similar trend, yet they exhibit no statistically significant difference between normal and perilesional lung tissue.

Typical results for the resolved concentration maps are shown in Fig. 3 for normal, perilesional, and cancerous lung tissue. The average concentrations of tryptophan, elastin, NADH, and FAD exhibit the overall monotonous decrease from normal, perilesional to cancerous tissue (Trp: 61.7, 40.6, and 22.8 mM; elastin: 15.2, 13.7, and 4.2 mM; NADH: 0.23, 0.22, and 0.19 mM; and FAD: 0.47, 0.35, and 0.19 mM for normal, perilesional, and cancerous lung tissue, respectively). The corresponding average concentration ratio is 0.0065, 0.0085, to 0.0053 for FAD/Trp and 2.00, 1.52, to 0.98 for FAD/NADH, respectively, well consistent with Table 1. The first column of Fig. 3 shows the corresponding hematoxylin and eosin (H&E) stained image from a different serial cut section of the same site. Note that the nuclei do not contain elastin, NADH, or FAD, evident in their corresponding concentration maps. The mitochondria are associated with elevated concentrations of NADH and FAD. The perilesional case is particularly clear, showing the abundance of mitochondria in NADH, FAD, and FAD/Trp maps. The appearance of moderate content of elastin over the cellular region in Fig. 3 may partially originate from the relative larger error in the recovery of elastin from NMF under the current experimental condition (see Table 2).

For better visualization, the extracted maps for different fluorophore species may be combined to yield a computationally stained image by color coding the fluorophore species. Figure 4 shows the computationally stained images for the normal, perilesional, and cancerous sites from the fluorophore concentration maps shown in Fig. 3. The fluorophore species Trp, elastin, NADH, and FAD are color coded as gray, green, blue, and yellow with their intensities proportional to the concentration, respectively. Compared with the conventional stained images, the computationally stained images exhibit distinctive advantages in highlighting the biochemical contrast between normal, perilesional, and cancerous sites. For example, the computationally stained images in Fig. 4 clearly show the abundance of Trp and elastin in the normal site and the shifting of the redox ratio, in particular over the mitochondria, between the perilesional and cancerous sites. The mitochondria are violet in the perilesional

Table 1 The concentrations (mM) of tryptophan, elastin, NADH, and FAD and the redox ratios (concentration ratios) of FAD/Trp and FAD/NADH measured for normal ($n = 36$), perilesional ($n = 30$), and cancerous ($n = 52$) lung tissue from 18 patients. The number inside the parenthesis is the standard deviation. The *p*-values are computed for normal versus perilesional (N–P), perilesional versus cancerous (P–C), and normal versus cancerous (N–C) with a *t*-test.

	Trp	Elastin	NADH	FAD	FAD/Trp	FAD/NADH
Normal	63(15)	23(19)	0.38(0.15)	0.43(0.13)	$7.6(1.8) \times 10^{-3}$	1.7(0.7)
Perilesional	44(10)	13(7)	0.24(0.06)	0.33(0.13)	$8.4(2.2) \times 10^{-3}$	2.0(1.0)
Cancerous	24(8)	9.1(4.9)	0.15(0.04)	0.14(0.05)	$6.5(2.5) \times 10^{-3}$	1.0(0.4)
p-value N–P	4×10^{-4}	0.006	1×10^{-5}	0.01	0.6	0.3
P–C	8×10^{-12}	9×10^{-4}	1×10^{-9}	3×10^{-15}	0.005	7×10^{-7}
N–C	1×10^{-19}	3×10^{-7}	1×10^{-16}	1×10^{-19}	0.009	0.0001

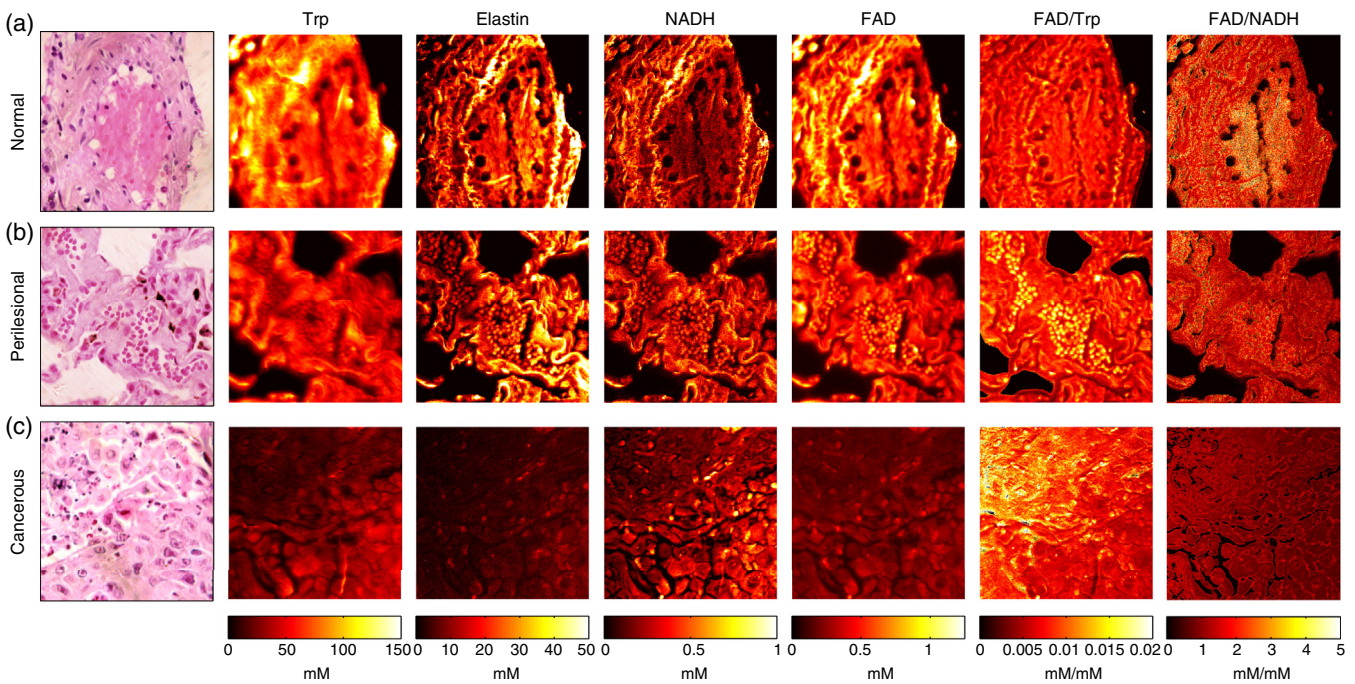

Fig. 3 The chemometric microscopic images for typical (a) normal, (b) perilesional, and (c) cancerous lung tissue. The first column shows the corresponding H&E stained image from a different serial cut section of the same site. The other columns from left to right are the concentrations (mM)of tryptophan, elastin, NADH, and FAD and the concentration ratios of FAD/Trp and FAD/NADH, respectively. The window size is 160 μm $\times$ 160 μm.

Table 2 The ratio of the recovered and the actual average concentrations and the similarity between the reconstructed and actual concentration maps under various noise levels. Map similarity is the 2-D image correlation coefficient with the value of unity meaning a perfect match.

	Avg. concentr. ratio				Map similarity			
Noise level (%)	Trp	Elastin	NADH	FAD	Trp	Elastin	NADH	FAD
1.0	1.08	0.74	1.08	1.03	0.95	0.64	0.98	1.00
0.5	1.06	0.80	1.05	1.02	0.97	0.81	0.99	1.00

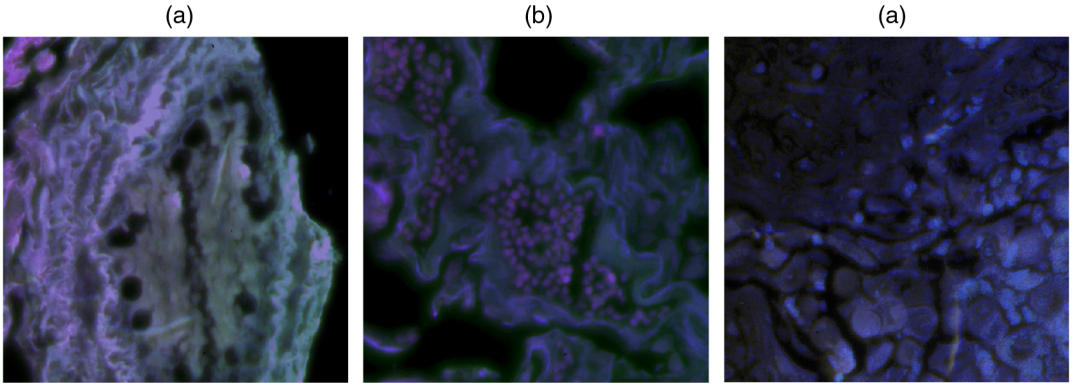

Fig. 4 The computationally stained images for the (a) normal, (b) perilesional, and (c) cancerous sites from the fluorophore concentration maps shown in Fig. 3. The fluorophore species Trp, elastin, NADH, and FAD are color coded as gray, green, blue, and yellow, respectively, with their intensities proportional to the concentration.

site and become blue in the cancerous site with the reduction in the redox ratio FAD/NADH.

A decrease in tryptophan concentration suggests accelerated catabolism and enhanced cytokine-induced degradation of tryptophan. This may reflect activation of tryptophan-degrading enzyme indoleamine (2,3)-dioxygenase at the tumor site, which may also be responsible for the lowering of the serum tryptophan concentration of lung cancer patients.[33] A similar trend in the reduction of tryptophan concentration with malignancy has been reported in human breast and fibroblast cell lines.[34,35] Elastin was found to be one main fluorophore in lung tissue, and a dramatic decrease in its fluorescence accompanying a disorganized fibered network was observed for precancer tissue compared with normal tissue.[36] Pitts et al.[15] found that the carcinogen-transformed cells showed an appreciable decrease in the fluorescence intensity of both NADH and flavins, and the punctate, spatial localization of the autofluorescence was lost compared with immortalized human bronchial epithelial cells. The same trends were observed here (see Table 1 and Fig. 3). The decreasing redox ratio FAD/NADH with cancer is well-known as the consequence of the Warburg effect.[37] It is worth noting here that not only the absolution concentration of both FAD and NADH decreases but also FAD decreases more significantly than all other fluorophores with cancer. This gives rise to the reduction of FAD/NADH and, further, the observed increasing percentage of NADH (and other non-FAD) fluorescence in the total detected signal (see Fig. 5). The ratio FAD/Trp exhibits a similar trend as FAD/NADH for lung tissue.

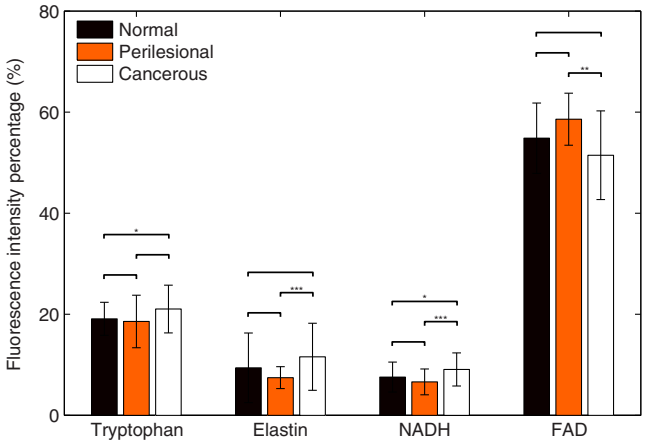

Fig. 5 The percentage of fluorescence intensities varies between normal ($n = 36$), perilesional ($n = 30$), and cancerous ($n = 52$) lung tissue. The significance is presented by "*" ($p < 0.05$), "**" ($p < 0.01$), and "***" ($p < 0.001$). The total fluorescence intensity is normalized to one.

Not much data on the absolute concentrations of endogenous fluorophores in tissue were reported in the literature. The concentration of tryptophan translates to a mass density of ~10 g/L, close to the mass fraction of ~1.2% of tryptophan in dry tissue.[38] The NADH concentration was reported to be in the range of ~0.2 to 1 mM in breast tissue.[39] A similar range of NADH concentration was found for breast cells[40] and esophageal cells.[41] Considering their different tissue types and alterations by tissue processing, the values in Table 1 fall within the reasonable range of fluorophore concentrations in processed tissue.

The chemometric method presented here is particularly suited when the spectra of the fluorescent species are not known exactly. Figure 6 shows that nonnegative factorization aided by the spatial diversity successfully recovers the fluorescence species, whereas the inversion with the inexact *a priori* spectra results in appreciable artifacts when the spectra are known inexactly and with a moderate amount of relative error of 5%.

The number of recoverable species of fluorophores is limited by m, the total number of excitation–detection channels. Additional channels need to be added to accommodate more species of fluorophore to be quantified. One potential issue of NMF is that it may yield nonunique solutions. This ambiguity is minimized using the known spectral signature of "pure" fluorophores as the initial guess of the feature matrix to the block principal pivoting NMF algorithm.[30,42] Furthermore, the satisfactory recovery of the fluorophore spectra and concentration depends on the SNR and the spectral distinctiveness between the underlying fluorophore species. To assess the uncertainties in the recovered concentrations, we performed numerical experiments by first synthesizing fluorescence images from given fluorophore concentrations and then extracting the fluorophore concentrations using the chemometric method after compounding with noise. Table 2 displays the ratio of the recovered and the actual average concentrations and the similarity

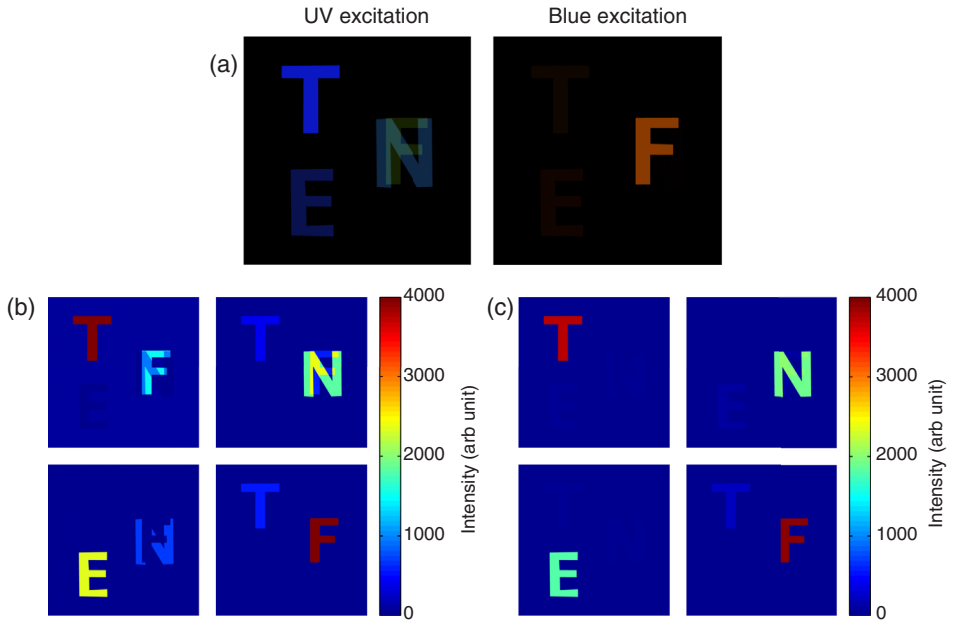

Fig. 6 Nonnegative factorization aided by the spatial diversity recovers the fluorescence species when the *a priori* spectra are only known inexactly. (a) Synthesized fluorescence images under UV and blue excitations compounded by 0.5% noise. (b) Recovered fluorescence species by inversion with the inexact *a priori* spectra (the negative values are set to zero). (c) Recovered fluorescence species with NMF. The relative error of the *a priori* spectra is 5%. The letter "T," "E," "N," and "F" represent Trp (intensity: 4000), elastin (intensity: 2000), NADH (intensity: 2000), and FAD (intensity: 4000), respectively.

(2-D correlation coefficient) between the reconstructed and actual concentration maps for the case where the fluorescence contribution from Trp, elastin, NADH, and FAD is 2:1:1:2, similar to that of human lung. The recovered Trp, NADH, and FAD concentration maps are more accurate, whereas that of elastin is least accurate as its fluorescence strength is weak and has a similar spectral signature to that of Trp. The noise in the measured fluorescence images was <1% in our experiments. One potential approach to improving the performance of the chemometric method is to optimize the NMF algorithm for the high spatial resolution and limited number of excitation–detection channels in chemometric fluorescence microscopy and incorporate spatial priors of the fluorophore distribution. This work is currently being investigated and will be reported in the future.

The quantification of individual fluorophore species in terms of their absolute fluorescence strength and concentration rather than a relative one is challenging, yet it has some important advantages. All other factors such as light absorption, scattering, and volume effects affecting the detected intensity of the fluorescence signal need to be meticulously taken into account. The potential uncertainties in system responses and measurement details that may affect the reported data and the observed fluorescence characteristics associated with the tissue physiological state can then be eliminated. An objective comparison between different methods becomes straightforward. Most importantly, the recovery of the absolute fluorophore concentration as biologically relevant data facilitates data interpretation and improves tissue diagnosis. Figure 5 shows the variation of the relative fluorescence strength with tissue type in contrast to that of the absolute strength given in Fig. 2. The discriminating power of the relative fluorescence strength is much weaker than that of the absolute fluorescence strength as suggested by their p-values for the statistical significance. Indeed, the absolute concentrations can be used to classify noncancer (perilesional and normal, $n = 66$) versus cancer ($n = 52$) much more accurately than the relative fluorescence strength. The receiver operating characteristic (ROC) curves computed using a support vector machine (SVM)[43] with fivefold cross validation are shown in Fig. 7 in which the accuracy of the classification is 99.8% for the former and 93.9% for the latter. The accuracy with the redox ratios alone is 77.1%.

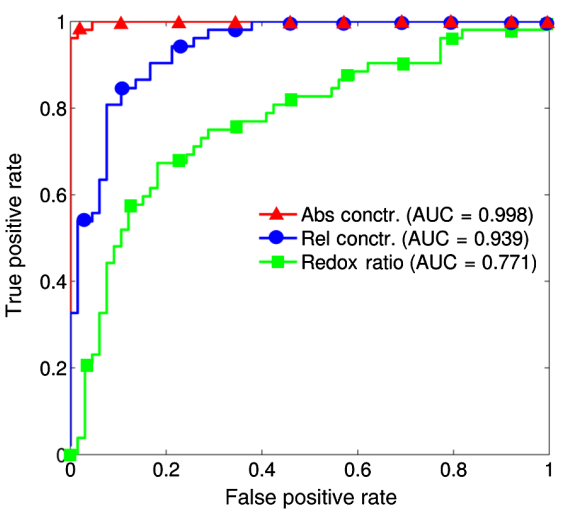

Fig. 7 The discrimination power of the absolute concentrations is much stronger than that of relative fluorescence strength and redox ratios. The ROC curves were computed using a SVM with fivefold cross validation for classification of noncancer (perilesional plus normal) versus cancer.

In conclusion, we have presented chemometric wide-field fluorescence microscopy for imaging the spatial distribution and concentration of endogenous fluorophores in thin tissue sections. Using broadband excitation and detection and nonnegative factorization aided by spatial diversity, both the spectral signature and the spatial distribution of endogenous fluorophores are recovered. The species and absolute concentration map of individual fluorophores are then derived by comparing the known "pure" fluorophore signature and their strength under the identical imaging condition. This microscopy has been demonstrated by retrieving the concentration map of all major endogenous fluorophores for normal, perilesional, and cancerous lung tissue. Chemometric fluorescence quantification in terms of the absolute concentration map rather than the relative strength exhibits some significant advantages including the elimination of the uncertainties due to system responses or measurement details, the generation of more biologically relevant data, and, most importantly, the enhancement in the accuracy of tissue diagnosis. This should also simplify the assessment of competing fluorescence imaging approaches.

Disclosures

The authors have no other relevant financial interests in this article and no potential conflicts of interest to disclose.

Acknowledgments

This work was supported in part by the National Nature Science Foundation of China Award# 81470081 and US DOD Award# W81XWH-10-1-0526. M. Xu reports a patent application related to the technology and analysis methods described in this study.

References

1. B. Chance, "Optical methods," *Annu. Rev. Biophys. Biophys. Chem.* **20**(1), 1–30 (1991).
2. J. W. Lichtman and J.-A. Conchello, "Fluorescence microscopy," *Nat. Methods* **2**, 910–919 (2005).
3. R. Alfano et al., "Laser induced fluorescence spectroscopy from native cancerous and normal tissue," *IEEE J. Quantum Electron.* **20**, 1507–1511 (1984).
4. R. Richards-Kortum and E. Sevick-Muraca, "Quantitative optical spectroscopy for tissue diagnosis," *Annu. Rev. Phys. Chem.* **47**, 555–606 (1996).
5. S. Schantz et al., "*In vivo* native cellular fluorescence and histological characteristics of head and neck cancer," *Clin. Cancer Res.* **4**, 1177–1182 (1998).
6. G. A. Wagnieres, W. M. Star, and B. C. Wilson, "*In vivo* fluorescence spectroscopy and imaging for oncological applications," *Photochem. Photobiol.* **68**(5), 603–632 (1998).
7. A. C. Croce et al., "Dependence of fibroblast autofluorescence properties on normal and transformed conditions. Role of the metabolic activity," *Photochem. Photobiol.* **69**, 364–374 (1999).
8. N. Ramanujam, "Fluorescence spectroscopy of neoplastic and non-neoplastic tissues," *Neoplasia* **2**(1–2), 89–117 (2000).
9. R. Alfano, "Stokes shift emission spectroscopy of human tissue and key biomolecules," *IEEE J. Sel. Top. Quantum Electron.* **9**, 148–153 (2003).
10. M. Monici, "Cell and tissue autofluorescence research and diagnostic applications," *Biotechnol. Annu. Rev.* **11**, 227–256 (2005).
11. J. M. Levitt et al., "Intrinsic fluorescence and redox changes associated with apoptosis of primary human epithelial cells," *J. Biomed. Opt.* **11**(6), 064012 (2016).
12. B. Wu, S. K. Gayen, and M. Xu, "Fluorescence spectroscopy using excitation and emission matrix for quantification of tissue native fluorophores and cancer diagnosis," *Proc. SPIE* **8926**, 89261M (2014).
13. A. Pradhan et al., "Steady state and time-resolved fluorescence properties of metastatic and non-metastatic malignant cells from different species," *J. Photochem. Photobiol. B* **31**, 101–112 (1995).
14. S. Andersson-Engels et al., "*In vivo* fluorescence imaging for tissue diagnostics," *Phys. Med. Biol.* **42**, 815–824 (1997).
15. J. D. Pitts et al., "Autofluorescence characteristics of immortalized and carcinogen-transformed human bronchial epithelial cells," *J. Biomed. Opt.* **6**, 31–40 (2001).
16. R. Drezek et al., "Autofluorescence microscopy of fresh cervical-tissue sections reveals alterations in tissue biochemistry with dysplasia," *Photochem. Photobiol.* **73**, 636–641 (2001).
17. I. Georgakoudi et al., "NAD(P)H and collagen as in vivo quantitative fluorescent biomarkers of epithelial precancerous change," *Cancer Res.* **62**, 682–687 (2002).
18. I. Pavlova et al., "Microanatomical and biochemical origins of normal and precancerous cervical autofluorescence using laser-scanning fluorescence confocal microscopy," *Photochem. Photobiol.* **77**, 550–555 (2003).
19. R. S. DaCosta et al., "Autofluorescence characterisation of isolated whole crypts and primary cultured human epithelial cells from normal, hyperplastic, and adenomatous colonic mucosa," *J. Clin. Pathol.* **58**, 766–774 (2005).
20. J. H. Ostrander et al., "Optical redox ratio differentiates breast cancer cell lines based on estrogen receptor status," *Cancer Res.* **70**, 4759–4766 (2010).
21. C. W. Groetsch, *The Theory of Tikhonov Regularization for Fredholm Equations of the First Kind*, Pitman, London (1984).
22. D. D. Lee and H. S. Seung, "Learning the parts of objects by non-negative matrix factorization," *Nature* **401**, 788–791 (1999).
23. P. Sajda et al., "Nonnegative matrix factorization for rapid recovery of constituent spectra in magnetic resonance chemical shift imaging of the brain," *IEEE Trans. Med. Imaging* **23**, 1453–1465 (2004).
24. J. Aubin, "Autofluorescence of viable cultured mammalian cells," *J. Histochem. Cytochem.* **27**, 36–43 (1979).
25. R. C. Benson et al., "Cellular autofluorescence—is it due to flavins?," *J. Histochem. Cytochem.* **27**, 44–48 (1979).
26. T. J. Staughton, C. J. McGillicuddy, and P. D. Weinberg, "Techniques for reducing the interfering effects of autofluorescence in fluorescence microscopy: improved detection of sulphorhodamine B-labelled albumin in arterial tissue," *J. Microsc.* **201**, 70–76 (2001).
27. M. Gu et al., "Effect of Handling and Fixation Processes on Two-Photon Autofluorescence Spectroscopy," in *Femtosecond biophotonics: core technology and applications*, pp. 9–32, Cambridge University Press, Cambridge, New York (2010).
28. M. W. Conklin et al., "Fluorescence lifetime imaging of endogenous fluorophores in histopathology sections reveals differences between normal and tumor epithelium in carcinoma in situ of the breast," *Cell Biochem. Biophys.* **53**, 145–157 (2009).
29. J. Adur et al., "Optical biomarkers of serous and mucinous human ovarian tumor assessed with nonlinear optics microscopies," *PLoS One* **7**, e47007 (2012).
30. J. Kim and H. Park, "Toward faster nonnegative matrix factorization: a new algorithm and comparisons," in *Proc. of the 2008 Eighth IEEE Int. Conf. on Data Mining*, pp. 353–362, IEEE (2008).
31. J. Jiang et al., "What is the space of spectral sensitivity functions for digital color cameras?," in *Proc. of IEEE Workshop on Applications of Computer Vision*, pp. 168–179, IEEE (2013).
32. J. A. Pierce and J. B. Hocott, "Studies on the collagen and elastin content of the human lung," *J. Clin. Invest.* **39**, 8–14 (1960).
33. A. B. Engin et al., "Increased tryptophan degradation in patients with bronchus carcinoma," *Eur. J. Cancer Care* **19**, 803–808 (2010).
34. G. M. Palmer et al., "Autofluorescence spectroscopy of normal and malignant human breast cell lines," *Photochem. Photobiol.* **78**(5), 462–469 (2003).
35. N. Grossman et al., "Fluorescence spectroscopy for detection of malignancy: H-ras overexpressing fibroblasts as a model," *J. Biochem. Biophys. Methods* **50**(1), 53–63 (2001).
36. L. Thiberville et al., "*In vivo* imaging of the bronchial wall microstructure using fibered confocal fluorescence microscopy," *Am. J. Respir. Crit. Care Med.* **175**(1), 22–31 (2007).
37. O. Warburg, "On the origin of cancer cells," *Science* **123**, 309–314 (1956).

38. J. R. Wiśniewski and F. Z. Gaugaz, "Fast and sensitive total protein and peptide assays for proteomic analysis," *Anal. Chem.* **87**(8), 4110–4116 (2015).
39. A. Uppal and P. K. Gupta, "Measurement of NADH concentration in normal and malignant human tissues from breast and oral cavity," *Biotechnol. Appl. Biochem.* **37**(Pt 1), 45–50 (2003).
40. Q. Yu and A. A. Heikal, "Two-photon autofluorescence dynamics imaging reveals sensitivity of intracellular NADH concentration and conformation to cell physiology at the single-cell level," *J. Photochem. Photobiol. B* **95**, 46–57 (2009).
41. S. Villette et al., "Ultraviolet-induced autofluorescence characterization of normal and tumoral esophageal epithelium cells with quantitation of NAD(P)H," *Photochem. Photobiol. Sci.* **5**(5), 483–492 (2006).
42. R. A. Neher et al., "Blind source separation techniques for the decomposition of multiply labeled fluorescence images," *Biophys. J.* **96**, 3791–3800 (2009).
43. C.-C. Chang and C.-J. Lin, "LIBSVM," *ACM Trans. Intell. Syst. Technol.* **2**, 1–27 (2011).

Biographies for the authors are not available.